A rad-hard CMOS active pixel sensor for electron microscopy

Marco Battaglia [a,b,*], Devis Contarato [b], Peter Denes [b], Dionisio Doering [b], Piero Giubilato [b,c,d], Tae Sung Kim [b], Serena Mattiazzo [c,d], Velimir Radmilovic [b], Sarah Zalusky [a,b]

[a] *Department of Physics, University of California at Berkeley, CA 94720, USA*
[b] *Lawrence Berkeley National Laboratory, Berkeley, CA 94720, USA*
[c] *INFN, Sezione di Padova, I-35131, Italy*
[d] *Dipartimento di Fisica, Università degli Studi, Padova I-35131, Italy*

ARTICLE INFO

ABSTRACT

Monolithic CMOS pixel sensors offer unprecedented opportunities for fast nano-imaging through direct electron detection in transmission electron microscopy. We present the design and a full characterisation of a CMOS pixel test structure able to withstand doses in excess of 1 Mrad. Data collected with electron beams at various energies of interest in electron microscopy are compared to predictions of simulation and to 1.5 GeV electron data to disentagle the effect of multiple scattering. The point spread function measured with 300 keV electrons is $(8.1 \pm 1.6)\,\mu m$ for $10\,\mu m$ pixel and $(10.9 \pm 2.3)\,\mu m$ for $20\,\mu m$ pixels, respectively, which agrees well with the values of 8.4 and $10.5\,\mu m$ predicted by our simulation.

1. Introduction

CMOS monolithic active pixel sensors were first proposed as photo-detectors 40 years ago. About a decade ago their use as charged particle detectors started to be explored, recognising that they represent an appealing technology offering small pixel size and the possibility of high speed readout [1,2]. In addition to their use in charged particle tracking, they have been proposed and investigated for direct electron detection in electron microscopy, in particular in Transmission Electron Microscopy (TEM) as electron imagers [3–5] together with hybrid pixels [6–8], as an advantageous alternative to CCDs optically coupled to phosphor plates (for a review of different detection technologies, see Ref. [9]).

For single particle tracking, it has been demonstrated that CMOS pixels of order $10 \times 10\,\mu m^2$ can reconstruct the position of impact of the particle with an accuracy of $\mathcal{O}(1\,\mu m)$, by using the centre of gravity of the charge distribution [10]. Owing to their thin sensitive region, confined to the $\simeq 10\,\mu m$ lightly doped epitaxial layer, these sensors can be back-thinned down to $\leqslant 50\,\mu m$, without loss in performance [11]. The thin charge-collection region and total thickness of CMOS pixel sensors is ideal in TEM applications, where multiple scattering effects are significant, for obtaining a good Point Spread Function (PSF). In

the energy region of interest in TEM, which is $\simeq 60 - 400\,keV$, the specific energy loss, dE/dx, varies by an order of magnitude but remains large enough to ensure single electron detection with large signal-to-noise ratio (S/N) values. For TEM, the detector should record the position of a collection of electrons that represents a magnified image. Whereas diffusion is beneficial for tracking applications, as it improves the determination of the charge centre of gravity, and thus of the particle impact point, to an accuracy significantly better than the pixel pitch, for TEM diffusion is harmful, as it increases the PSF and needs to be carefully evaluated.

While significant progress has been made in the last few years to develop CMOS pixel sensors for tracking and vertexing applications in particle collider experiments, several issues, relevant to their application for fast nano-imaging at TEM, remain to be addressed. In particular, their radiation hardness is a key challenge in the design of a detector for TEM. Unlike HEP, where the total dose requirement can be estimated, based on integrated luminosity, TEM requirements depend on the mode of operation. Whereas the radiation hardness for the specimen can be easily specified (in electrons per square angstrom), as the magnification is variable, this does not translate into a requirement on the detector. In addition, large numbers of electrons may be contained in a limited number of Bragg spots, when operating in diffraction mode, causing large doses to be received by a small number of pixels. Given that a very intense bright field image could deposit order of $10\,rad\,s^{-1}\,pixel^{-1}$, a target radiation tolerance of $\geqslant 1\,Mrad$ would enable its use for approximately one year, which appears to be a valid requirement.

* Corresponding author at: Lawrence Berkeley National Laboratory, Berkeley, CA 94720, USA. Tel.: +1 510 486 7029.
E-mail address: MBattaglia@lbl.gov (M. Battaglia).

In this paper we present a prototype CMOS active pixel sensor with radiation tolerant pixel cell design for use in TEM. We evaluate its performance applying high energy physics (HEP) modelling and experimental techniques to their characterisation as TEM detectors. We study the particle energy loss, charge spread, PSF and response after irradiation with 200 keV electrons and 29 MeV protons for doses in excess to 1 Mrad. Data are compared to results of detailed simulation of electron interactions, energy loss and signal generation.

2. Sensor design and readout

We developed a new circuit, named LDRD2-RH, optimised for radiation tolerance, as a variation on a previous circuit, developed for HEP applications [12]. The LDRD2-RH chip retains the original addressing and output circuitry. The sensor is divided into several sectors, each consisting of 24×48 pixels arrayed on a 20 μm pitch, in order to test different pixel layouts. The principle radiation damage mechanism is radiation-induced leakage current in the charge-collecting diode. This leakage current is primarily caused by the positive potential generated by trapped (positive) charge in the oxide above the p-type silicon, which results in inversion of the silicon at the Si/SiO₂ interface. In each $20 \times 20 \, \mu m^2$ pixel, two $10 \times 20 \, \mu m^2$ pixels are drawn: each with the same design of the charge-collecting diode, and with the classical 3T-readout. For both sub-pixels, the transistor sizes (W/L) are the same, but in one sub-pixel the transistor has a conventional linear layout, and in the other, an enclosed gate layout. Fig. 1 shows some of the different diode layouts used. The detector has been fabricated in the AMS 0.35 μm 4-metal, 2-poly CMOS-OPTO process, which has an epitaxial layer with a nominal thickness of 14 μm.
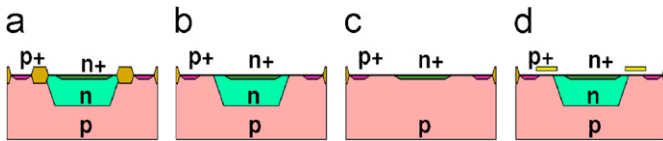

Fig. 1. Cross-section layouts of different diodes used in the test chip. The diode in (a), GR, is an n-well diode with an enclosing $p+$ guard ring; (b) NW draws thin oxide over the diode; (c) is like (b) but without the well implant; and (d) PO is like (b) but with a polysilicon ring covering the potentially inverted region.
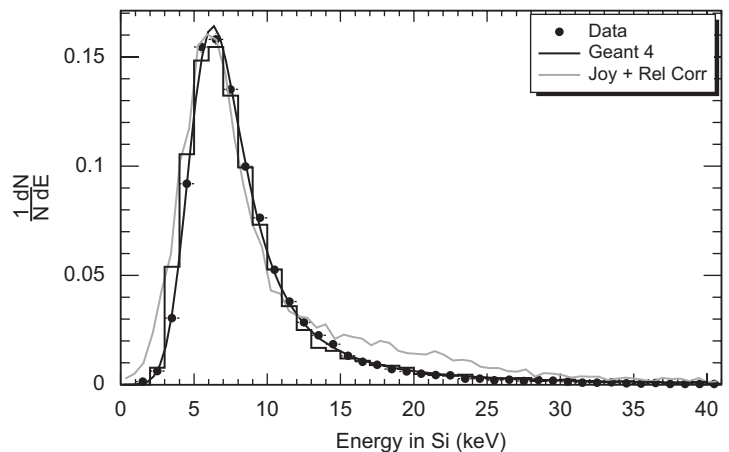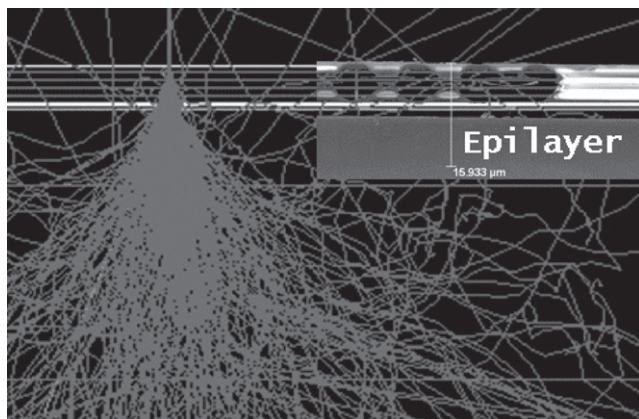
Pixels are read out in rolling shutter mode, which ensures a constant integration time across the pixel matrix. Pixels are clocked at 6.25 and 25 MHz, corresponding to an integration time of 737 and 184 μs, respectively. The detector is read out through a custom FPGA-driven acquisition board. A set of 14 bits, 40 MSample s⁻¹ ADCs reads the chip outputs, while an array of digital buffers drives all the required clocks and synchronisation signals. The FPGA has been programmed to generate the clock pattern and collect the data sampled by the ADCs. A 32 bit-wide bus connects the FPGA to a National Instruments PCI 6533 digital acquisition board installed on the PCI bus of a control PC. Data is processed on-line by a LabView-based program, which performs the computation of the pixel noise and pedestal levels. Results are given for the PO pixel design, which was found to be best performing in terms of radiation tolerance, read out at 6.25 MHz, unless otherwise noted.

3. Response simulation

The energy deposition in the sensor active layer and the lateral charge spread is simulated using two independent programs.

The simulation of electron scattering in matter for applications in electron microscopy has been described in Ref. [13]. The first simulation program is inspired by this formalism, but with the relativistic corrections added, as required for accuracy at our energies of interest. The second simulation is based on the `Geant-4` program [14] and uses the low energy electromagnetic physics models [15].

In both simulations, the CMOS sensor is modelled according to the detailed geometric structure of oxide, metal interconnect and silicon layers, as specified by the foundry. Electrons are incident perpendicular to the detector plane and tracked through the sensor. For each interaction within the epitaxial layer, the energy released and the position are recorded. Fig. 2 shows the sensor layout adopted in the simulation with the simulated trajectories of 200 keV electrons.

The two simulation programs give a good description of the measured energy deposition as shown in Fig. 2. `Geant-4` provides with a better description of the high energy part of the Landau distribution which tends to be systematically over-estimated by the results of the first simulation program. This effect becomes more significant with increasing electron energies.

Fig. 2. Response simulation of the LDRD2-RH chip. (Left) Simulated trajectories of 200 keV electrons in the pixel sensor. The metal layers on top and the sensitive epitaxial layer below are highlighted. (Right) Reconstructed deposited energy for 200 keV electrons. The points with error bars show the data, the grey smoothed line the prediction of the simulation according to Ref. [13] with relativistic corrections added and the histogram the result of the `Geant-4` simulation. The continuous line is the fit to the data points with a Landau function convoluted with a Gaussian noise term.

Table 1
Lateral charge spread due to multiple scattering predicted by `Geant-4` for various electron energies

E_e	Lateral spread (μm)
120 keV	15.6
160 keV	11.5
200 keV	9.3
300 keV	6.8
1.5 GeV	1.3

The lateral charge spread due to multiple scattering in the sensor is evaluated in simulation by computing the lateral position of the electron interaction points in the epitaxial layer, weighted by the deposited energy. Results from the `Geant-4` simulation are given in Table 1.

Charge collection is simulated with `PixelSim`, a dedicated digitisation module [16], developed in the `Marlin C++` reconstruction framework [17]. This processor starts from the ionisation points generated along the particle trajectory by `Geant-4` and models the diffusion of charge carriers from the epitaxial layer to the collection diode. `PixelSim` provides us with full simulation of the response of all the individual pixels in the detector matrix, including electronics noise and efficiency effects, which can be processed through the same analysis chain as the data. The simulation has a free parameter, the diffusion parameter σ_{diff}, used to determine the width of the charge carrier cloud, which is tuned to reproduce the pixel multiplicity in the cluster measured for 1.5 GeV electrons in data, as discussed in the next section. We find the best agreement between the simulated and measured pixel multiplicity in the cluster for $\sigma_{\text{diff}} = 16.5\,\mu$m. This can be compared with an estimate of the charge diffusion length $L_n = \sqrt{D_n \tau_n}$, obtained from the diffusion coefficient, $D_n = kT/e\mu_n$, and the charge-collection time, τ_n. The diffusion coefficient is computed for an estimated doping of $10^{14} - 10^{15}$ cm^{-3} of the epitaxial layer. The charge-collection time has been measured on data. We focus a 1060 nm laser to a $\simeq 10\,\mu$m spot onto a single pixel and pulse the laser for 2 ns. The pixel analog output is recorded on a digital oscilloscope and we observe that the pixel analog level reaches a plateau 150 ns after the arrival of the laser pulse. From these data we estimate a diffusion length of $14 - 19\,\mu$m, which agrees well with the simulation result.

4. Sensor tests

4.1. Energy deposition

The detector calibration is obtained by recording the position of the 5.9 keV full energy peak of a collimated 2.2 mCi ^{55}Fe source. We find a conversion factor of 0.98 keV/ADC count or 26.7 e$^-$/ADC count at 6.25 MHz readout frequency.

Electrons in the energy range from 120 to 200 keV from the 200CX electron microscope at the National Center for Electron Microscopy (NCEM) are used to characterise the detector response to low energy particles. The response to high momentum particles is studied with the 1.5 GeV electron beam extracted from the LBNL Advanced Light Source (ALS) booster. Data are converted into the `lcio` format [18]. Data analysis is performed offline by a set of dedicated processors developed in `Marlin` and proceeds as follows. Events are first scanned for noisy pixels. The noise and pedestal values computed on-line are updated, using the algorithm in Ref. [19], to follow possible variations in the course of data taking. The measured average pixel noise is (130 ± 6) e$^-$ and (71 ± 4) e$^-$ of equivalent noise charge (ENC) for the electron microscope and the ALS data, respectively, at 6.25 MHz and (110 ± 8) e$^-$ and (67 ± 5) e$^-$ at 25 MHz. The noise is partly due to the readout electronics, and is larger in the electron microscope set-up due to the longer cable needed to route the analog signals out of the vacuum enclosure at the bottom of the microscope column, with a minor contribution from leakage current from operating the detector at $\simeq +25\,°$C.

Electron hits are then reconstructed from the recorded pixel pulse heights. The detector is scanned for pixels with pulse height values over a given S/N threshold. These are designated as cluster 'seeds'. Seeds are sorted according to their pulse heights and the surrounding neighbouring pixels are tested for addition to the cluster. The neighbour search is performed in a 5×5 matrix around the seed. Pixel thresholds at 3.5 and 2.0 units of noise have been used for seed and additional pixels, respectively. Clusters are not allowed to overlap, i.e. pixels already associated with one cluster are not considered for populating another cluster around a different seed. Finally, we require that clusters are not discontinuous, i.e. pixels associated to a cluster cannot be interleaved by any pixel below the neighbour threshold. Reconstructed hits are characterised in terms of the energy recorded in a 3×3 pixel matrix centred around the seed pixel, the pixel multiplicity of the reconstructed cluster and the fraction of the total charge collected by the pixels in the matrix, sorted in order of decreasing pulse height.

Results for the reconstructed deposited energy are shown in Fig. 3, where data and simulation for 120, 160, 200 keV and 1.5 GeV electrons are compared. The simulation reproduces well the measured energy deposition, over this range of particle energies. The observed average values of energy deposition exceeds those predicted by the thin straggling model [20] for 14 μm of Si, due to the effect of electron interactions in the SiO$_2$ and metal layers on top of the sensitive volume.

4.2. Charge spread

The lateral charge spread is studied from the shape of the reconstructed clusters. The two variables used are the cluster size, i.e. the average pixel multiplicity $\langle N_{\text{pixels}} \rangle$, and the distribution of the fraction of the total charge collected in the pixels with the highest pulse height in a matrix around the seed pixel. Table 2 compares the cluster size for electrons of different energies measured in data with the simulation prediction. The cluster size for 1.5 GeV electrons is governed by the charge carrier diffusion in the epitaxial layer, since the multiple scattering is negligible compared to the pixel size, at this energy. Both data and simulation show an increase of the multiplicity for lower energies consistent with the combined effect of the larger collected charge, which pushes the pulse height on more pixels above the S/N threshold for additional pixels, and of the multiple scattering in the detector, which displaces the locations of energy deposition from the point of entrance of the electron. The two effects can be disentangled by analysing the fraction of the cluster charge collected in the pixels with the highest pulse height in a 3×3 matrix around the cluster seed. Fig. 4 shows the results obtained for data at 120 and 200 keV compared to 1.5 GeV electrons. We indeed observe an increase of the area over which the charge spreads with 120 keV electrons, consistent with the effect of lateral charge spread due to multiple scattering which becomes of the order of the pixel size. On the contrary there is no significant increase on the charge distribution for 200 keV electrons, where we also observe only a very modest increase in cluster size. These results are well reproduced by simulation as shown in Fig. 4. This first validation of simulation in the description of charge spread is
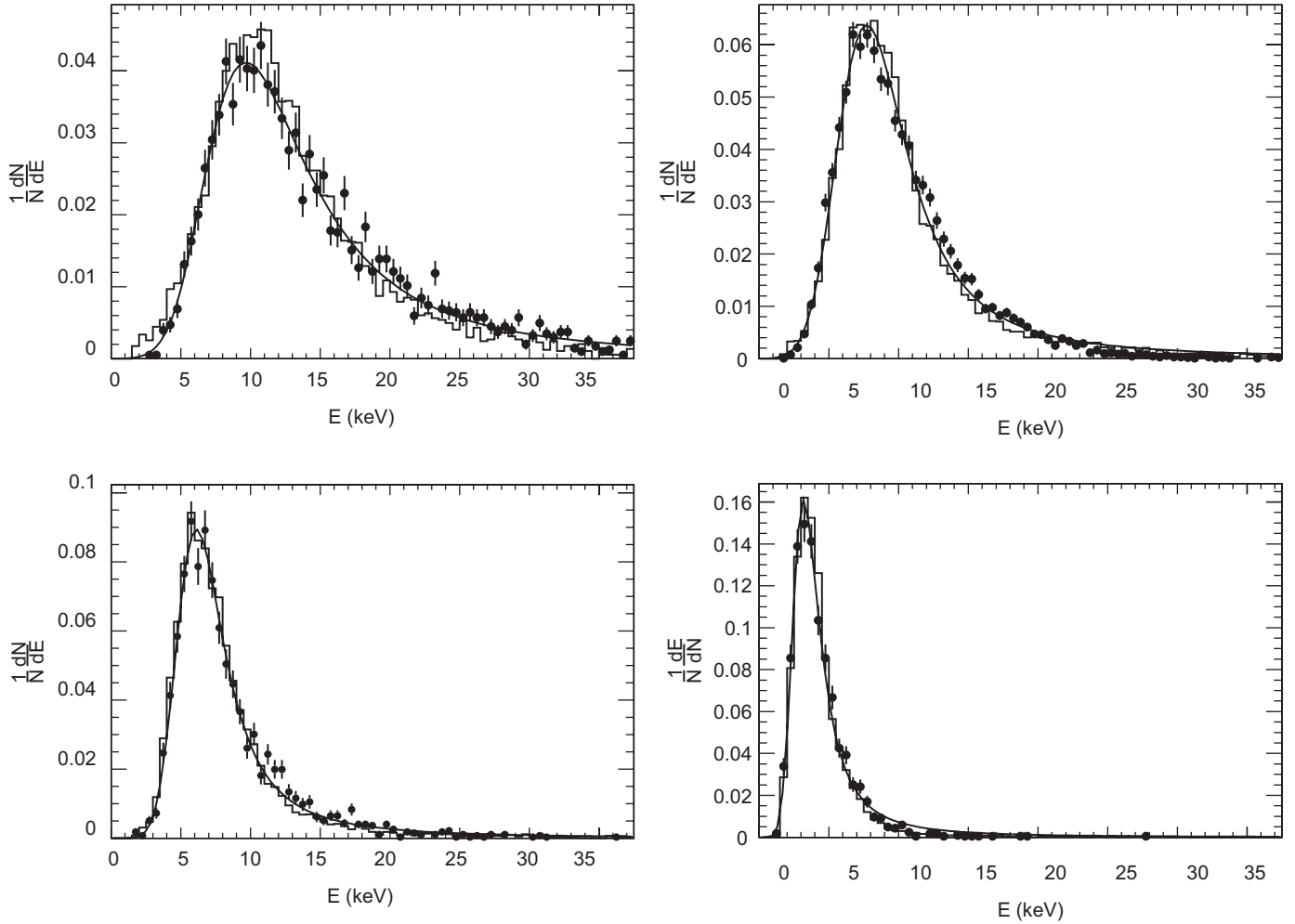
Fig. 3. Reconstructed deposited energy in the 3×3 pixel matrix for 120 keV electrons (upper left), 160 keV electrons (upper right), 200 keV electrons (lower left) and 1.5 GeV electrons (lower right). The points with error bars show the data and the histogram the result of the `Geant-4` simulation. The continuous line shows a Landau function convoluted with a Gaussian noise term fit to the data.

Table 2
Cluster size for electrons of different energies in data and simulation

E_e	$\langle N_{pixels} \rangle$ data	$\langle N_{pixels} \rangle$ simulation
120 keV	3.35 ± 0.06	3.01 ± 0.02
160 keV	2.82 ± 0.04	2.73 ± 0.03
200 keV	2.25 ± 0.04	2.33 ± 0.03
1.5 GeV	2.20 ± 0.02	2.21 ± 0.02

important for its use in the PSF estimation, which is discussed next.

4.3. PSF and imaging

The detector PSF originates from charge spread due to charge carrier diffusion and ionising particle scattering, as well as by the finite spatial sampling frequency, which depends on the pixel pitch. We estimate the PSF using `Geant-4 + PixelSim` simulation and test the simulation results with data. In simulation, a monochromatic, point-like beam of electrons is sent onto the surface of the detector. The point spread function is determined as the r.m.s. of the predicted distribution of the detected charge on the pixels. Results are summarised in Table 3 for different electron
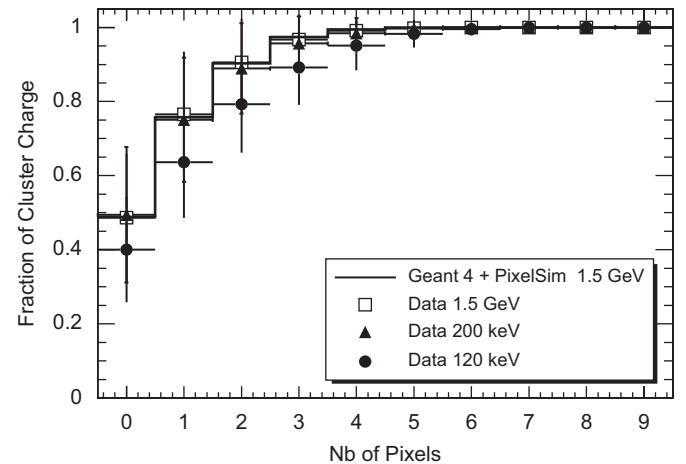

Fig. 4. Fraction of the charge collected in a 3×3 pixel matrix as a function of the number of pixels added, for 120 keV (dots), 200 keV (triangles), 1.5 GeV (squares) data, and 1.5 GeV simulation (line). The error bars show the r.m.s. of the data distribution. Pixels in the matrix are sorted in decreasing pulse height order.

energies and 10 and 20 μm pixel pitch. Simulation predicts a PSF better than 10 μm for 300 keV electrons imaged with a 10 μm pixel pitch.
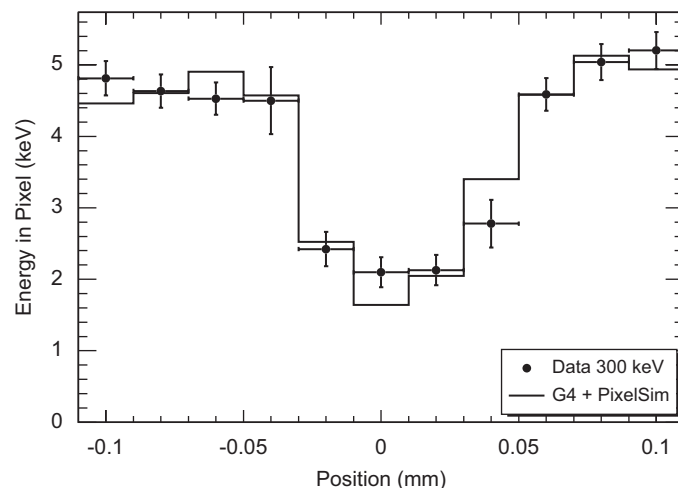
We validate these results using data taken at different energies, from 100 up to 300 keV, with 10 and 20 μm pixels at the TITAN test column at NCEM. We use the LDRD2-RH as well as an earlier sensor, the LDRD1 chip, featuring simple 3T pixels with 10, 20 and 40 μm pitch and fabricated in the same AMS 0.35-OPTO process [21]. A gold wire was mounted, parallel to the pixel columns, at a distance of ≃ 3 mm from the detector surface. The wire diameter is measured to be (59.6 ± 0.7) μm, using a high resolution optical survey system. Since the gold wire has well-defined edges, the profile of the deposited energy in the pixels, measured across the wire allows us to study the charge spread due to scattering and diffusion along the projected image of the wire edge and compare to simulation.

The set-up has been simulated in detail in Geant-4 and the pixel response extracted from PixelSim. We study the change in the recorded signal, by scanning along pixel rows across the gold wire. Fig. 5 shows the pulse heights measured on the pixels along a set of rows, comparing data at 300 and 120 keV with simulation, for the 20 μm pixel pitch. The good agreement observed validates the estimation of the point spread function obtained from simulation.

Further, we extract the point spread function directly from the data and compare the results to the simulation predictions. We parametrise the measured pulse height on pixel rows across the image projected by the wire with a box function smeared by a Gaussian term, which describes the point spread function. The maximum and minimum pulse height levels, for pixels away from the wire region and for the pixel exactly below the wire centre, respectively, are fixed to those observed in data and we perform a simple 1-parameter χ^2 fit to extract the Gaussian width term, which gives the PSF. At 300 keV, we measure a PSF value of (8.1 ± 1.6) μm for 10 μm pixels on the LDRD1 chip (see Fig. 6) and of (10.9 ± 2.3) μm for 20 μm pixels on the LDRD2-RH chip, to be compared to simulation which predicts 8.4 and 10.5 μm, respectively. The PSF scaling with electron energy and pixel size is

shown in Fig. 6. Again data and simulation are in good agreement. It is interesting to observe that for increasing electron energies the point spread function improves, due to the reduction of multiple
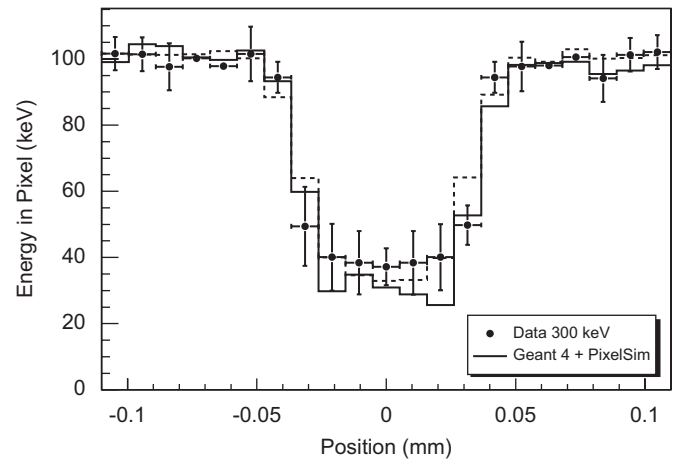

Fig. 6. Point spread function determination. Top: Pulse heights measured on pixels with 10 μm pitch, along a row across the Au wire stretched above the 10 μm pixels of the LDRD1 sensor for 300 keV beam. Data (points with error bars) are compared with the prediction of the Geant-4 + PixelSim (solid line) simulation and the box+Gaussian function fit (dashed line). Bottom: PSF as a function of beam energy. Data (points with error bars) are compared to simulation (lines) for 10 and 20 μm pixels.

Table 3
Point spread function predicted by Geant 4 + PixelSim for different electron energies and 10 and 20 μm pixel pitch

Energy (keV)	10 μm pixels	20 μm pixels
120	11.4	13.1
200	9.1	11.2
300	8.4	10.5

Fig. 5. Pulse heights measured on pixels with 20 μm pitch, along a row across the Au wire stretched above the LDRD2-RH sensor. Data at 300 keV (left) and 120 keV (right) are compared with the prediction of the Geant-4 + PixelSim simulation.
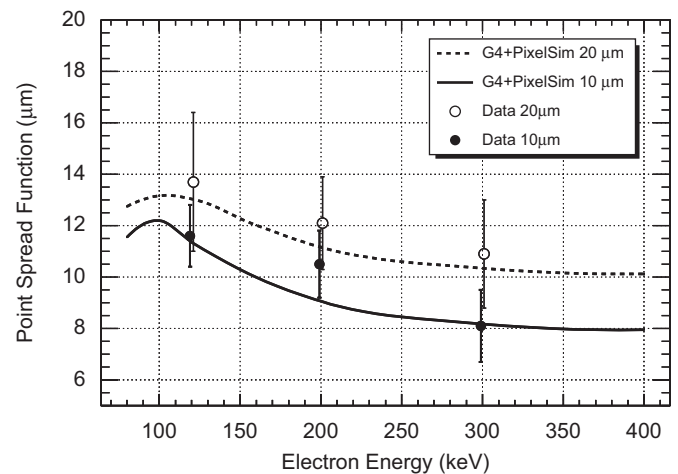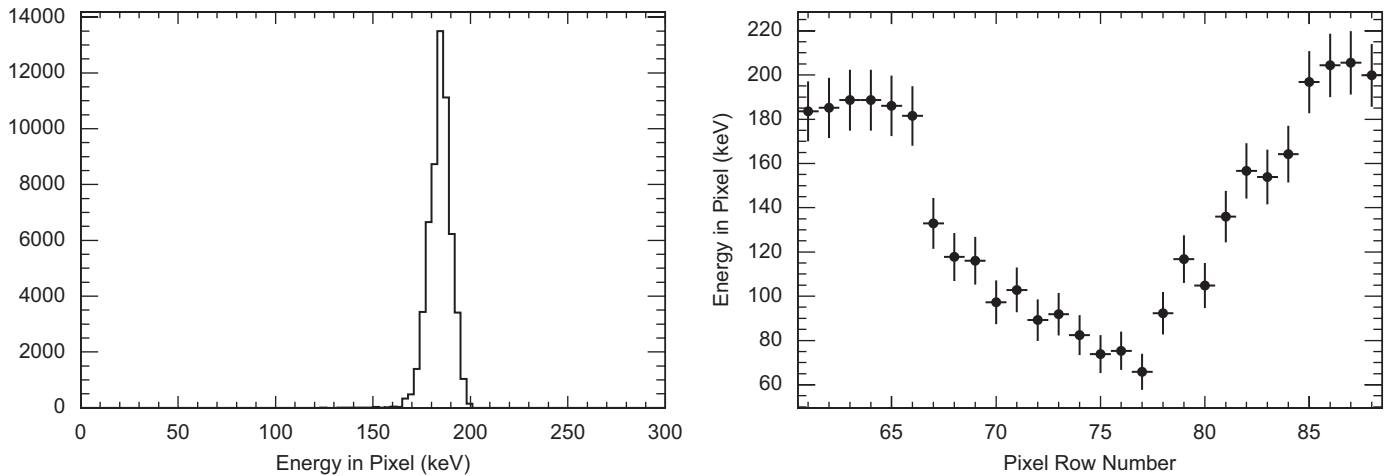
Fig. 7. (Left) Energy recorded on individual pixels with 200 keV electrons flat field illumination, (right) energy recorded on a pixel column across the projected image of a Pb–Sn alloy nanoparticle in an Al matrix.
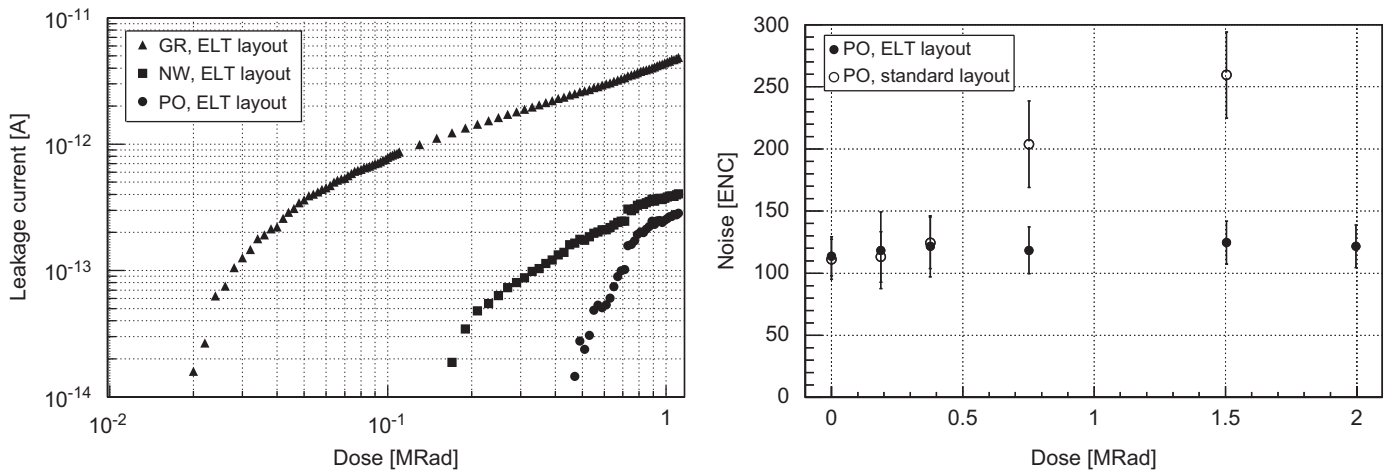

Fig. 8. Results of the LDRD2-RH sensor irradiation. (Left) Sensor leakage current as a function of dose for 200 keV electrons. (Right) Average pixel noise as a function of dose for 29 MeV proton in cells designed with ELT and standard layouts. The measurement at the highest dose for the standard layout is not reported since the sensor output signal saturated the ADC dynamic range due to the increased pixel leakage current. The error bars represent the r.m.s. of the pixel noise distributions.

scattering, up to $\simeq 300$ keV, where it approaches an asymptotic value for 10 μm pixels, dominated by the effect of charge spread and spatial sampling frequency. On the opposite end of the energy range, the point spread function grows to a maximum around 100 keV and simulation predicts it to fall for lower energies, due to the short range in Si of these soft electrons.

Finally, we have performed a realistic imaging test with the LDRD2-RH sensor, by acquiring images of nanoparticles of a 91.8% Pb + 8.2% Sn alloy embedded in a solid Al matrix [22] at the 200CX electron microscope. The images are obtained with a 200 keV electron flat field illumination at 6.25 MHz readout frequency and 50 frames s^{-1} are written to disk. We estimate the flux to be $\simeq 35$ e$^-$ pixel^{-1} event^{-1}, where one event corresponds to a 737 μs integration time. Fig. 7 shows the pulse height recorded on the pixels across the projected image of a nanoparticle.

5. Sensor irradiation

The radiation tolerance of the LDRD2-RH chip for use in TEM has been assessed by comparing the sensor response before and after irradiation with 200 keV electrons up to a dose in excess of 1 Mrad. Results have been integrated by an irradiation with

29 MeV protons at the LBNL 88-in. cyclotron. We study the pixel noise, leakage current and charge collection. All tests are performed at room temperature.

For the electron irradiation, the sensor active surface has been covered with a same gold mesh, having 50 μm wide bars and 204 μm wide holes. This allows to compare the response of irradiated and non-irradiated pixels on the same chip. The sensor has been irradiated with a flux of $\simeq 2300$ e$^-$ s^{-1} μm^{-2}, in multiple steps, up to a total estimated dose of 1.11 Mrad. In between consecutive irradiation steps, 100 events are acquired without beam and the pixel pedestals and noise computed, in order to monitor the evolution of the pixel leakage current with dose. Fig. 8 shows the increase of the pixel pedestal levels, which measure the leakage current, as a function of the integrated dose.

After irradiation the sensor response is tested with 200 keV and 1.5 GeV electrons. The deposited energy in the 3×3 pixel matrix is compared to that obtained before irradiation. We fit the energy spectrum with a Landau function convoluted with a Gaussian distribution to represent the noise contribution. The fit function has three free parameters, the Landau peak position (Landau m.p.v.), the Gaussian width (Gaussian noise) and an overall normalisation. Due to the large correlation between the Gaussian width and the Landau width, the latter is fixed in the fit
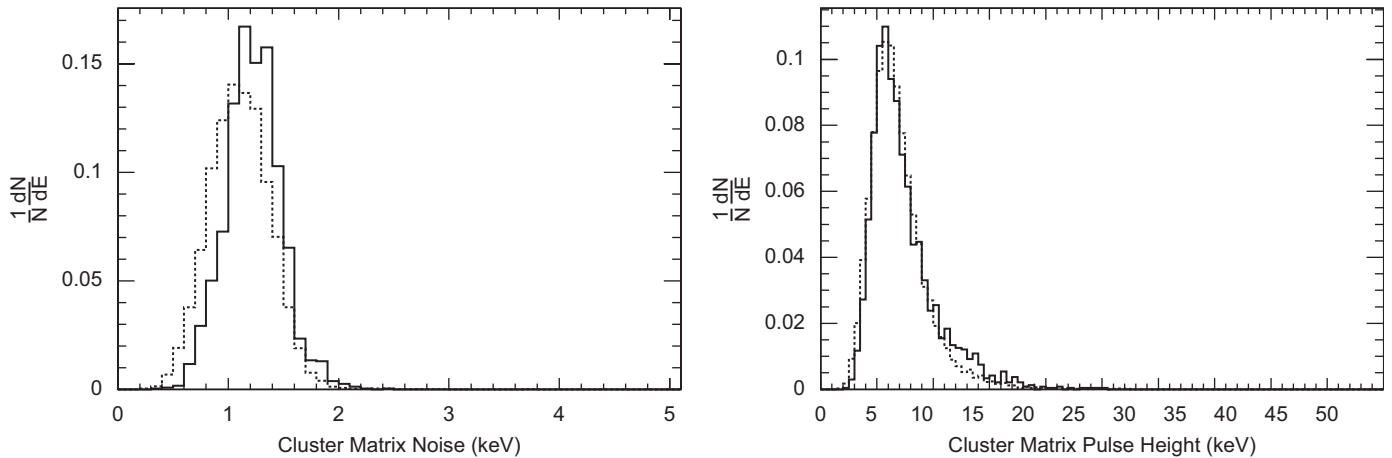
Fig. 9. Measured noise (left) and deposited energy (right) in a 3 × 3 pixel matrix for 200 KeV electrons before (continuous line) and after (dashed line) irradiation, obtained after applying the gain correction described in the text.

Table 4
Results of the fits to the distributions of the deposited energy in a 3 × 3 pixel matrix for 200 keV and 1.5 GeV electrons before and after the 1.1 Mrad electron irradiation

	Before irradiation (keV)	After irradiation (keV)
200 keV e⁻		
Landau m.p.v.	(5.57 ± 0.04)	(5.54 ± 0.04)
Gaussian noise	(1.19 ± 0.04)	(0.98 ± 0.03)
3 × 3 matrix noise	(1.22 ± 0.20)	(1.11 ± 0.20)
1.5 GeV e⁻		
Landau m.p.v.	(3.05 ± 0.03)	(3.37 ± 0.07)
Gaussian noise	(0.60 ± 0.06)	(0.81 ± 0.07)
3 × 3 matrix noise	(0.74 ± 0.01)	(0.88 ± 0.01)

The noise of the 3 × 3 pixel matrix is also given for comparison. Data after the irradiation is re-calibrated to account for the observed gain shift.

to the value obtained on simulation. We observe a change of the gain by $\simeq 1.35$, confirmed by calibration with ^{55}Fe. After correcting for this gain shift, the noise and energy deposition distributions before and after irradiation are in good agreement. In the ALS data, taken with shorter connections between the detector and the digitiser board, the electronics noise is lower and an hint of a small increase of the detector noise after irradiation may be observed. The deposited energy spectrum is unchanged after irradiation, confirming that the charge-collection properties of the pixel cell are not affected. Results are summarised in Fig. 9 and Table 4.

Since the threshold energy for electrons to cause displacement damage in silicon is 260 keV [23], we expect 200 keV to create only ionising damage. We investigated the effect of 29 MeV protons, which damage the sensor via both ionisation and non-ionising energy loss. The irradiation has been performed at the BASE Facility of the LBNL 88-in. cyclotron [24]. Results are reported in details in Ref. [25]. One prototype sensor was irradiated with 29 MeV protons up to a total integrated fluence of 8.5×10^{12} pixel cm^{-2}, corresponding to a total dose of $\simeq 2$ Mrad. At equal doses, a larger increase of the leakage current, compared to the electron irradiation, hints at a probable contribution from displacement damage. Fig. 8 (right) shows the average pixel noise in the PO sectors for ELT and linear transistors; it can be seen that while the noise of the ELT layout cells remains basically unchanged over the dose range and only slightly increases at the highest doses, the noise of the standard layout cells is doubled after ∼1 Mrad. The increased leakage current can be controlled by cooling the chip. The PO design with ELT layout

appears to be the most radiation tolerant of the designs tested in the LDRD2-RH chip.

6. Conclusions

Thin monolithic CMOS pixel sensors with small, radiation tolerant pixels offer a very attractive solution for fast nano-imaging in transmission electron microscopy. The thin sensitive layer ensures a direct detection with small multiple scattering contribution to the point spread function. Fast readout and single electron sensitivity in small pixel cells result in high resolution dynamic imaging. We have developed a prototype CMOS pixel sensor implementing radiation tolerant cells. The sensor response in terms of energy deposition, charge spread and point spread function has been extensively tested for electrons in the energy range of interest for TEM. A detailed simulation based on `Geant-4` and a dedicated charge generation and collection simulation package has been validated on the data recorded.

The point spread function measured with 300 keV electrons is $(8.1 \pm 1.6)\,\mu m$ for $10\,\mu m$ pixel and $(10.9 \pm 2.3)\,\mu m$ for $20\,\mu m$ pixels, respectively, which agrees well with the values of 8.4 and $10.5\,\mu m$ predicted by our simulation.

The radiation tolerance of pixels with enclosed transistors and specific diode design has been verified with 200 keV electrons and 29 MeV protons. The pixel cells withstand doses in excess to 1 Mrad, without significant degradation in noise and charge collection efficiency, making them well suited for a sensor for direct detection in TEM.

References

[1] E.R. Fossum, IEEE Trans. Electron. Devices ED-44 (1997) 1689.
[2] R. Turchetta, et al., Nucl. Instr. and Meth. A 458 (2001) 677.
[3] A.-C. Milazzo, et al., Ultramicroscopy 104 (2005) 152.
[4] G. Deptuch, et al., Ultramicroscopy 107 (2007) 674.

[5] P. Denes, J.-M. Bussat, Z. Lee, V. Radmillovic, Nucl. Instr. and Meth. A 579 (2007) 891.

[6] G.Y. Fan, et al., Ultramicroscopy 70 (1998) 113.

[7] A.R. Faruqi, D.M. Cattermole, C. Reburn, Nucl. Instr. and Meth. A 513 (2003) 317.

[8] A.R. Faruqi, et al., Ultramicroscopy 94 (2003) 263.

[9] A.R. Faruqi, R. Henderson, Curr. Opinion Struct. Biol. 17 (2007) 549.

[10] Yu. Gornushkin, et al., Nucl. Instr. and Meth. A 513 (2003) 291.

[11] M. Battaglia, D. Contarato, P. Giubilato, L. Greiner, L. Glesener, B. Hooberman, Nucl. Instr. and Meth. A 579 (2007) 675.

[12] M. Battaglia, et al., IEEE Trans. Nucl. Sci. 55 (6) (2008), doi:10.1109/TNS.2008.2007484.

[13] D. Joy, in: Monte Carlo Modeling for Electron Microscopy and Microanalysis, Oxford University Press, New York, 2005.

[14] S. Agostinelli, et al., Nucl. Instr. and Meth. A 506 (2003) 250.

[15] S. Chauvie, G. Depaola, V. Ivanchenko, F. Longo, P. Nieminen, M.G. Pia, Prepared for CHEP'01: Computing in High-Energy Physics and Nuclear, Beijing, China, 3–7 September 2001.

[16] M. Battaglia, Nucl. Instr. and Meth. A 572 (2007) 274.

[17] F. Gaede, Nucl. Instr. and Meth. A 559 (2006) 177.

[18] F. Gaede, T. Behnke, N. Graf, T. Johnson, in: Proceedings of the 2003 Conference for Computing in High-Energy and Nuclear Physics (CHEP 03), La Jolla, CA, 24–28 March 2003, TUKT001 [arXiv:physics/0306114].

[19] V. Chabaud, et al., Nucl. Instr. and Meth. A 292 (1990) 75.

[20] H. Bichsel, Nucl. Instr. and Meth. B 52 (1990) 136.

[21] M. Battaglia, et al., in: Proceedings of the International Symposium on Detector Development for Particle, Astroparticle and Synchrotron Radiation Experiments (SNIC 2006), Menlo Park, CA, 3–6 April 2006, ECONF-C0604032, p. 0108.

[22] H. Gabrisch, L. Kjeldgaard, E. Johnson, U. Dahmen, Acta Mater. 49 (2001) 4259.

[23] G. Lindström, Nucl. Instr. and Meth. A 512 (2003) 30.

[24] M.A. McMahan, Nucl. Instr. and Meth. B 241 (2005) 409.

[25] M. Battaglia, et al., IEEE Trans. Nucl. Sci. (2008), submitted for publication.